

# First-principles study of ferroelectric domain walls in multiferroic bismuth ferrite

Axel Lubk,<sup>1</sup> S. Gemming,<sup>2</sup> and N. A. Spaldin<sup>3</sup>

<sup>1</sup>*Institute for Structure Physics, Technische Universität Dresden, D-01062, Germany\**

<sup>2</sup>*Institute of Ion-Beam Physics and Materials Research, FZ Dresden-Rossendorf, D-01328 Dresden†*

<sup>3</sup>*Materials Department, University of California, Santa Barbara, CA, 93106-5050, USA‡*

(Dated: March 4, 2022)

We present a first-principles density functional study of the structural, electronic and magnetic properties of the ferroelectric domain walls in multiferroic BiFeO<sub>3</sub>. We find that domain walls in which the rotations of the oxygen octahedra do not change their phase when the polarization reorients are the most favorable, and of these the 109° domain wall centered around the BiO plane has the lowest energy. The 109° and 180° walls have a significant change in the component of their polarization perpendicular to the wall; the corresponding step in the electrostatic potential is consistent with a recent report of electrical conductivity at the domain walls. Finally, we show that changes in the Fe-O-Fe bond angles at the domain walls cause changes in the canting of the Fe magnetic moments which can enhance the local magnetization at the domain walls.

PACS numbers: 77.80.Dj, 77.84.Dy, 75.50.Ee

## I. INTRODUCTION

Perovskite-structured bismuth ferrite, BiFeO<sub>3</sub>, is the subject of much current research because of its large room temperature ferroelectric polarization and simultaneous (antiferro-)magnetic ordering. Such *multiferroic* materials show a wealth of complex physical properties caused by their coexisting electrical and magnetic order parameters, which in turn suggest potential applications in novel magnetoelectronic devices: Recent reports of electric-field induced switching of magnetization through exchange bias of ferromagnetic Co to BiFeO<sub>3</sub> are particularly promising [1, 2]. In addition, the large ferroelectric polarization [3], driven by the stereochemically active Bi<sup>3+</sup> lone pair [4], is motivating investigation of its purely ferroelectric behavior for possible applications in ferroelectric memories.

The suitability of ferroelectric materials for applications is determined not only by the magnitude of their ferroelectric polarization, but also by factors such as switchability, fatigue and loss. These are in turn influenced by the structure of the domains and particularly by the boundaries between them. The detailed structure and formation energies of domain walls in some conventional ferroelectrics are now well established (see for example Refs. 5, 6 for experimental studies and Refs. 7, 8 for calculations). For BiFeO<sub>3</sub>, however, the first experimental study of domain walls was only recently reported [9], and a detailed theoretical study is lacking. The additional consideration of the effect of the ferroelectric domain wall on the electronic and magnetic degrees of freedom makes such a study particularly compelling.

In this work we use density functional theory within the LSDA+*U* method to calculate the structure, stability and properties of the ferroelectric domain walls in BiFeO<sub>3</sub>. We begin this manuscript by reviewing the

structure of bulk BiFeO<sub>3</sub> (Section II), so that we can use the bulk symmetry to determine the allowed energetically favorable domain wall orientations (Section III). In Section IV we describe the technical details of our density functional calculations. The main part of the paper – Section V – contains our results: We perform full structural optimizations of the atomic positions for the energetically favorable domain wall orientations, and calculate and compare their total energies to determine which walls are most likely to occur. We then calculate the electronic and magnetic properties of the walls, paying particular attention to how changes in structure at the boundaries influence the electronic densities of states, potential profile and spin canting. The implications of our findings for domain walls in multiferroics, and suggestions for future directions are summarized in Section VI.

## II. STRUCTURE OF BiFeO<sub>3</sub>

BiFeO<sub>3</sub> is a rhombohedral perovskite with space group *R3c* (Fig. 1). The ground state structure is reached from the ideal cubic perovskite (*Pm3m*) by imposing two symmetry-adapted lattice modes: (1) a non-polar *R*-point mode which rotates successive oxygen octahedra in opposite sense around the [111]-direction, and (2) a polar  $\Gamma_4^-$  distortion, consisting of polar displacements along the [111]-direction as well as symmetric breathing of adjacent oxygen triangles [10]. The rhombohedral lattice constant is 5.63 Å (with corresponding pseudocubic lattice constant,  $a_0 = 3.89$  Å), and the rhombohedral angle,  $\alpha = 59.35^\circ$  is close to the ideal value of  $60^\circ$  [11]. First-principles density functional calculations have been shown to accurately reproduce these values [4].

The magnetic ordering is well established to be G-type antiferromagnetic [12], with a long wavelength

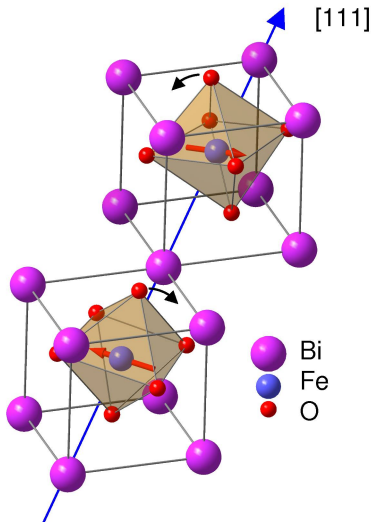


FIG. 1: Crystal structure of bulk  $\text{BiFeO}_3$ . Two simple perovskite unit cells are shown to illustrate that successive oxygen octahedra along the polar  $[111]$  axis rotate with opposite sense around  $[111]$ . The red arrows on the Fe atoms indicate the orientation of the magnetic moments in the  $(111)$  plane.

spiral of the antiferromagnetic axis [13]. First-principles density functional computations [14] and symmetry considerations [15] indicate a local canting of the magnetic moments to yield a weak ferromagnetic moment; this canting is symmetry allowed because of the presence of the non-polar  $R$  point rotations of the oxygen octahedra. Since the orientation of the weak ferromagnetic moment follows the axis of the long-range spiral no net magnetization results.

The ferroelectric polarization is large,  $\sim 90 \mu\text{C}/\text{cm}^2$  [3], and can point along any of the eight pseudo-cubic  $\langle 111 \rangle$  directions [11]. Simple geometrical considerations therefore suggest angles of  $\pm 71^\circ$ ,  $\pm 109^\circ$  or  $180^\circ$  between allowed polarization orientations of the ideal rhombohedral system ( $\alpha = 60^\circ$ ) [16]; we will label our domain walls using these angles in the following. Experimentally, such relative domain orientations and re-orientation angles have indeed been observed [1]. Currently nothing is known about the behavior of the octahedral rotations or the magnetism at the domain boundaries.

### III. SYMMETRY ANALYSIS OF DOMAIN WALLS

In general, the energetically favorable domain wall configurations for a particular symmetry are those

orientations which can be free of both stress and space charge. For the rhombohedral symmetry of  $\text{BiFeO}_3$ , these conditions lead to the following likely domain wall orientations for  $\pm 71^\circ$ ,  $\pm 109^\circ$  and  $180^\circ$  orientations respectively:  $\{011\}$ ,  $\{001\}$  and  $\{011\}$  (in pseudo-cubic coordinates) [16]. For each of these wall orientations, there is a choice of atomic plane about which the initial domain wall can be centered (for example around a  $\text{BiO}$  or  $\text{FeO}_2$  plane in the  $109^\circ$  case). In addition, since the rotations of the oxygen octahedra are uncoupled from the orientation of the polarization, different relative orientations of oxygen octahedra on either side of the domain wall are possible. In order to survey all possibilities we investigate the following domain boundaries:

1.  $71^\circ$ : We construct the domain wall in the  $(011)$  plane with the electric polarization changing from the  $[111]$  direction on one side of the domain wall to  $[\bar{1}11]$  on the other (Fig. 2(a)). We study two configurations of the rotations of the oxygen octahedra, which we refer to as either *continuous* or *changing*. In the continuous case, the phase of the oxygen octahedral rotations remains unchanged along an integral curve of the polarization vector field; in the changing case the phase reverses at the domain wall. In principle the wall could be centered around either a  $\text{BiFeO}$  or  $\text{O}_2$  plane (or any intermediate plane). However, since the domain wall location is not fixed by symmetry and the distance between the two planes is small, the fully relaxed domain boundary will likely be centered close to the  $\text{O}_2$  plane independent of the initial configuration (as found in Ref. [8]).
2.  $109^\circ$ : We use the  $(001)$  plane for the domain wall, with polarization changing from the  $[111]$  to the  $[\bar{1}\bar{1}1]$  direction (Fig. 2(b)). Again we explore two configurations of the octahedral rotations, with continuous or changing phase along the integral curve of the polarization vector field. In this case we were able to separately resolve domain walls centered on  $\text{FeO}_2$  and  $\text{BiO}$  planes, since their separation is  $\sqrt{2}$  times that of the  $\text{BiFeO}$  and  $\text{O}_2$  planes in the  $71^\circ$  case.
3.  $180^\circ$ : We use the  $(0\bar{1}1)$  plane for the domain wall, with polarization changing between  $[111]$  and  $[\bar{1}\bar{1}\bar{1}]$  directions (Fig. 2(c)). Again we explore two octahedral tilt patterns, with the phases along the polarization direction either continuous or changing across the boundary. As in the  $71^\circ$  case, we do not distinguish between the  $\text{BiFeO}$ - and  $\text{O}_2$ -centered domain walls.

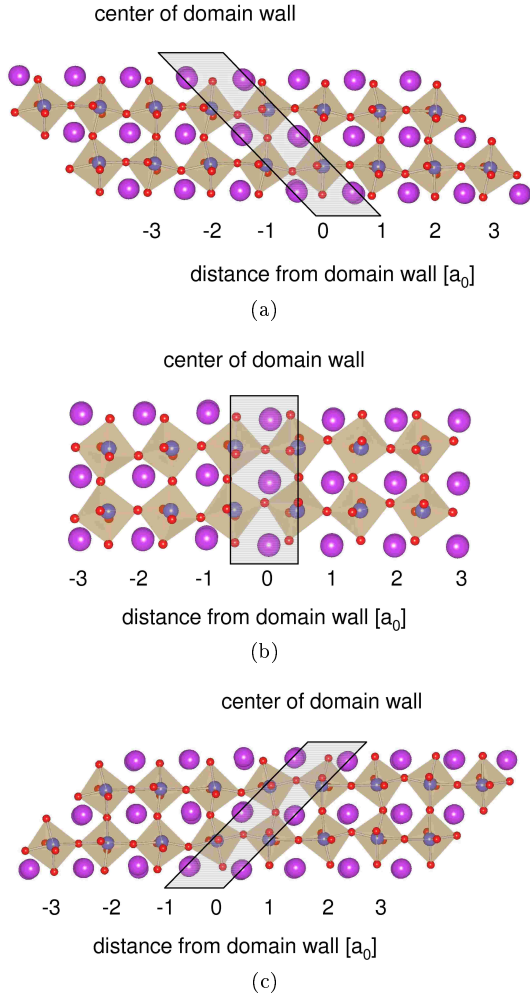


FIG. 2: (a) 71° domain boundary with continuous oxygen octahedral rotations. (b) 109° domain boundary with continuous oxygen octahedral rotations centered on the  $\text{FeO}_2$  plane. (c) 180° domain boundary with continuous oxygen octahedral rotations. Note that only half of the supercell is shown.

#### IV. COMPUTATIONAL DETAILS

We performed density functional (DFT) calculations using the Vienna *ab-initio* simulation package, VASP [17]. We used the projector augmented wave method [18, 19] with the default VASP PAW potentials including semi-core states in the valence manifold (core states Bi: [Kr], Fe: [Ne]3s<sup>2</sup>, O: 1s<sup>2</sup>). We used the rotationally invariant implementation [20] of the LSDA+U method [21] to describe the exchange-correlation functional with values of  $U = 3$  eV and  $J = 1$  eV that were shown previously to accurately reproduce the experimentally observed structural and electronic properties of bulk  $\text{BiFeO}_3$  [4, 14, 22].

We constructed supercells containing two domains separated by domain walls, with a total of 120 atoms

(60 atoms per domain); the width of each domain was then six pseudocubic unit cells. We used the lattice parameters obtained from calculations for bulk  $\text{BiFeO}_3$  (see Ref. 4), with a slight change: the rhombohedral angle,  $\alpha$ , was taken to be exactly 60° to allow us to incorporate both domains in one supercell. While the electronic structure of bulk  $\text{BiFeO}_3$  at  $\alpha = 60^\circ$  is indistinguishable from that at the experimental  $\alpha = 59.35^\circ$  [4], we point out that this constraint might influence the strain profile at the domain boundary. The total energy difference of bulk  $\text{BiFeO}_3$  with  $\alpha = 60^\circ$  and with  $\alpha = 59.35^\circ$  is below 1 meV, hence we conclude, that the effect may be neglected in the further discussion. We initialized the magnetic ordering to the *G*-type antiferromagnetic arrangement known to occur in the bulk.

Full structural optimizations of the atomic positions (until the forces on each ion were below 0.03 eV per Å) and cell parameters (until energy differences were below 0.01 eV) were then performed for all of the domain configurations described in Section III. No symmetry constraints were imposed. The cell parameter relaxations were necessary because the interlayer distance in all three domain walls is slightly larger (by around 0.1 Å) than that in the bulk. The rather large remaining forces occur due to a combination of the complicated crystal structure of  $\text{BiFeO}_3$  and the large number of atoms in one supercell, leading to a flat energy surface and a particularly slow structural convergence. Additionally, special care had to be taken with respect to the starting conditions of the structure optimization, i.e. several different initializations of the initial spin configuration and ion positions were performed for each configuration to reduce the probability of being trapped in local minima. We used  $5 \times 3 \times 1$  (71° and 180°) and  $5 \times 5 \times 1$  (109°) *k*-point samplings; these correspond to values that have been shown to give good convergence for bulk  $\text{BiFeO}_3$ , with a denser sampling along the long axis of the supercell. The plane wave energy cut-off was set to 550 eV.

Finally, for the calculated lowest energy 109° boundary, we performed additional non-collinear magnetic calculations with spin-orbit coupling included.

#### V. RESULTS

##### A. Structure and energetics

In all cases our supercells relaxed to contain two distinct domains, with the layers in the middle of each domain having similar structure to that of bulk  $\text{BiFeO}_3$ ; this suggests that the supercells were large enough to minimize interactions between the domain walls.

In Table I we list our calculated domain wall energies for all of the configurations described in the previous

71° c	71° d	109° Bc	109° Bd	109° Fc	109° Fd	180° c
363	436	205	896	492	1811	829

TABLE I: Calculated domain wall energies (mJ/m<sup>2</sup>) for 71°, 109° and 180° walls. B and F indicate the BiFeO<sub>3</sub>- and FeO<sub>2</sub>-centered planes, c and d label the continuous or discontinuous oxygen octahedral rotations.

section. It is clear that, in all cases, the configuration with the least perturbation to the phase of the octahedral rotations is lowest in energy. Indeed, in the 180° case we were unable to obtain a converged solution for the case with reversal of the octahedral rotations at the domain boundary. The large differences between the continuous and discontinuous oxygen octahedra rotations is a peculiarity of the BiFeO<sub>3</sub> structure and indicates the importance of the Fe-O-Fe bonding angles in determining the structural stability. The 109° wall is energetically the most stable of the three orientations. It is somewhat surprising that the 109° wall is lower in energy than the 71° wall; since the change in orientation of the electric polarization vector is smaller in the latter, one would also expect the perturbation to the structure to be smaller. (Previous calculations for PbTiO<sub>3</sub> found the 90° wall to be lower in energy than the 180° wall, consistent with this argument [8]). We believe that this reversal is caused by the favorable arrangement of the oxygen octahedra at the 109° wall boundary: since the 109° wall lies in the {001} plane, it is oriented along the apices of the oxygen octahedra (Fig. 2(b) upper panel), whereas the 71° and 180° {011} walls are oriented along the octahedral edges (Figs. 2(a) and 2(c) upper panels) giving them less freedom to accommodate the changes in polarization direction. The 109° BiO-centered wall is lower in energy than the FeO<sub>2</sub>-centered wall, consistent with previous studies for other perovskite ferroelectric domain boundaries which also found AO-centered walls to be more stable [8]. The 180° case has the highest domain wall energy, consistent with its having the largest change in the polarization orientation. Finally, we note that the domain wall energies in BiFeO<sub>3</sub> are significantly larger than those calculated for PbTiO<sub>3</sub>, which in turn are larger than the BaTiO<sub>3</sub> values (Table II). The large increase from BaTiO<sub>3</sub> to PbTiO<sub>3</sub> suggests a correlation between polarization magnitude and domain wall energy. While changes in polarization would predict somewhat larger domain wall energies for BiFeO<sub>3</sub>, there is a large additional increase which is likely a result of the additional deformations caused by the octahedral rotations (see discussion above). It is also possible that the magnetic energy cost associated with perturbing the Fe-O-Fe bond angles further raises the domain wall energies in BiFeO<sub>3</sub>.

As a measure of the amount of structural distortion, in Figure 3 we plot the Fe-O-Fe angles in each layer across

angle	BaTiO <sub>3</sub>	PbTiO <sub>3</sub>
90°	N/A	35.2
180°	7.5	132

TABLE II: Lowest calculated domain wall energies (mJ/m<sup>2</sup>) for 90° and 180° domain walls in BaTiO<sub>3</sub> and PbTiO<sub>3</sub>, from Ref. 8.

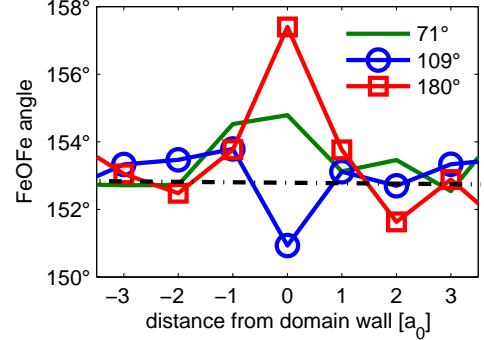


FIG. 3: Fe-O-Fe angles in each layer of the supercell. The bulk value of 152.9° is indicated by the dashed line. Note the changes in angle in the domain wall region.

the supercells. Within the central region of the domain the bulk value of 152.9° is regained as expected. Indeed the bulk behavior is recovered within one or two layers of the domain wall boundary, consistent with earlier studies on PbTiO<sub>3</sub> domain walls [8]. The angles change by up to ~4° in the wall region to accommodate the changes in structure associated with the polarization reorientation. However, the Fe-O-Fe angles remain far from 180° in all cases, indicating that the structure within the walls is far from an ideal cubic perovskite structure. Since the Fe-O-Fe angle strongly influences the superexchange interactions and the local anisotropy, we anticipate that these changes in angles might influence the magnetic properties; we return to this point later.

## B. Evolution of the polarization across the domain walls

In order to better understand the change in structure across the domain wall we performed a layer-by-layer analysis of the local polarization by summing over the displacements of the atoms in each layer from their ideal cubic perovskite positions, multiplied by their Born effective charges (BECs). While there is not a unique way to partition the layers, we find that our results from different decomposition schemes are similar, and so we use the narrowest possible layer partition in order to optimize the resolution. We used the BECs of the *R3c* structure calculated in a previous study [4] using the same computational parameters as we use here;

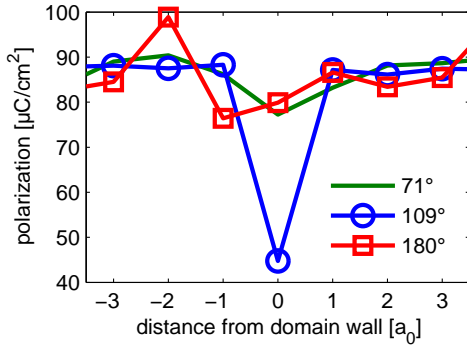


FIG. 4: Layer-by-layer polarization calculated from the sum of the displacements of the ions from their ideal positions multiplied by the Born effective charges.

note that the actual BECs might deviate slightly from these values. This technique was used previously to analyze the polarization evolution across  $\text{PbTiO}_3$  domain walls [8]. We are particularly interested in two factors: First whether the polarization reorientation takes place through a rigid rotation of the local polarization, without a reduction in its local magnitude (analogous to the rotation of a magnetic moment in a Bloch wall in a ferromagnet). And second, whether a change in polarization in the direction perpendicular to the wall develops. This is of particular interest since, as discussed in earlier work [8], it gives rise to a potential step at the boundary which, if screened by a dipole layer in the charge density, could give rise to intriguing effects such as enhanced conductivity at the boundary.

First, in Fig. 4 we show the *magnitudes* of the calculated layer-by-layer polarizations for all three wall types. It is clear that in the  $71^\circ$  and  $180^\circ$  walls, the magnitude of the polarization remains approximately constant across the wall, indicating a rigid rotation of the polarization in the manner of a magnetic Bloch wall. (Note that the scatter in the local polarization especially at the  $180^\circ$  results from our fairly high force tolerance of 0.03 eV per Å.) In contrast, the  $109^\circ$  wall has a marked reduction in the local polarization in the wall region; this likely results from the greater structural flexibility provided by the orientation of the  $109^\circ$  wall relative to the corners of the octahedra.

Next we analyze the local polarization by decomposing it into the components parallel and perpendicular to the planes of the domain walls. (Figs. 5(a), (b) and (c) for the  $71^\circ$ ,  $109^\circ$  and  $180^\circ$  walls respectively.) The total polarization in the mid-domain regions is  $\sim 90 \mu\text{C}/\text{cm}^2$  in all cases, in good agreement with previously reported bulk values [4]. In all cases the component parallel to the domain wall changes from its full mid-domain value in one orientation to the full value in the other orientation within two or three layers. The magnitude of the change in polarization component perpendicular

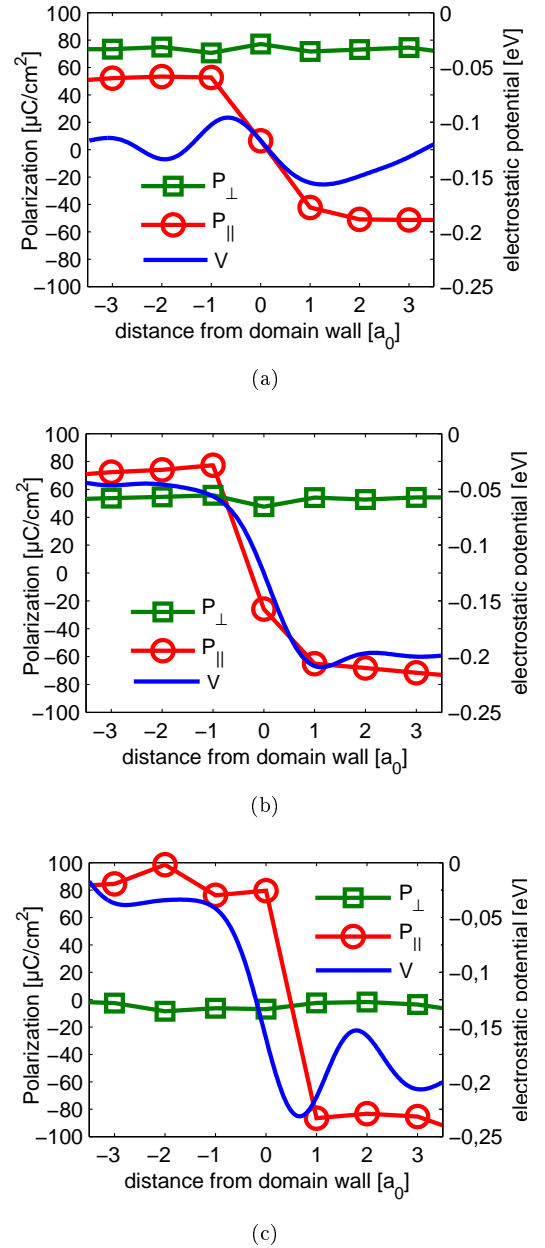


FIG. 5: Parallel and normal components of the polarization,  $P_{||}$  and  $P_{\perp}$ , and the macroscopically and planar averaged electrostatic potential,  $V$  for (a)  $71^\circ$  domain boundary with continuous oxygen octahedral rotations, (b)  $109^\circ$  domain boundary with continuous oxygen octahedral rotations centered on the  $\text{FeO}_2$  plane and (c)  $180^\circ$  domain boundary with continuous oxygen octahedral rotations. Note that only half of the supercell is shown.

to the wall, however, depends strongly on the domain wall type. In Figs. 5(a), 5(b) and 5(c) we also plot the planar and macroscopically averaged electrostatic potential (extracted as in Ref. [8]) across the supercell to illustrate the potential step associated with this change in perpendicular component of the polarization. For the

71° wall the change in perpendicular component and corresponding potential step are small; the magnitude of the potential step is  $\sim 0.02$  eV. In the 109° case the change in the in-out-of-plane component is considerable, and the corresponding step is significant (0.15 eV). This behavior is analogous to that reported previously in calculations for 90° domain walls [8]. Perhaps surprisingly, the 180° boundary shows the largest potential step, of 0.18 eV. (Earlier studies of 180° domain boundaries in tetragonal  $\text{PbTiO}_3$  [8] included an inversion center at the domain wall and therefore obtained no change in perpendicular component). The following analysis of the evolution of the polarization through successive corners of the pseudocube explains the loss of inversion symmetry and the change in the perpendicular component in the 180° case.

Interestingly, the presence of the large potential steps at the 109° and 180° walls, and the absence of a step at the 71° wall, correlate with an intriguing recent observation of electrical conductivity at the 109° and 180° walls, and its absence at the 71° wall [9]. A possible explanation of the observed conductivity is the generation of a space charge layer in the region of the wall to screen this otherwise energetically unfavorable potential discontinuity.

Finally, to help with visualizing the change in polarization across the domain walls, in Fig. 6 we indicate the local polarization vectors in each layer of the supercells as blue arrows showing the magnitude and orientation. In the 71° case we can clearly see that the polarization rotates from one corner of the pseudocubic unit cell, through the center of the edge to the adjacent corner, accompanied by the small attenuation in magnitude which we saw earlier in Fig. 4. As already seen in Fig. 5(a), this geometry allows the perpendicular component of polarization to remain constant across the wall. The analogous cartoon for the 180° wall (Fig. 6(c)) shows that the polarization vector rotates between successive corners of the pseudocubic unit cell which are the stable orientations of the polarization in  $R3c$   $\text{BiFeO}_3$ . At the layer-by-layer level of resolution we see a jump by 71° followed by a jump of 109°; both intermediate orientations have small components perpendicular to the domain wall. Note that imposition of an inversion center during the structural relaxation, which might be anticipated for a 180° wall, would not have allowed this ground state to develop. In contrast, the change in orientation of the polarization across the 109° wall is accompanied by a rather large attenuation of the total polarization (see Fig. 4 and Fig. 6(b)).

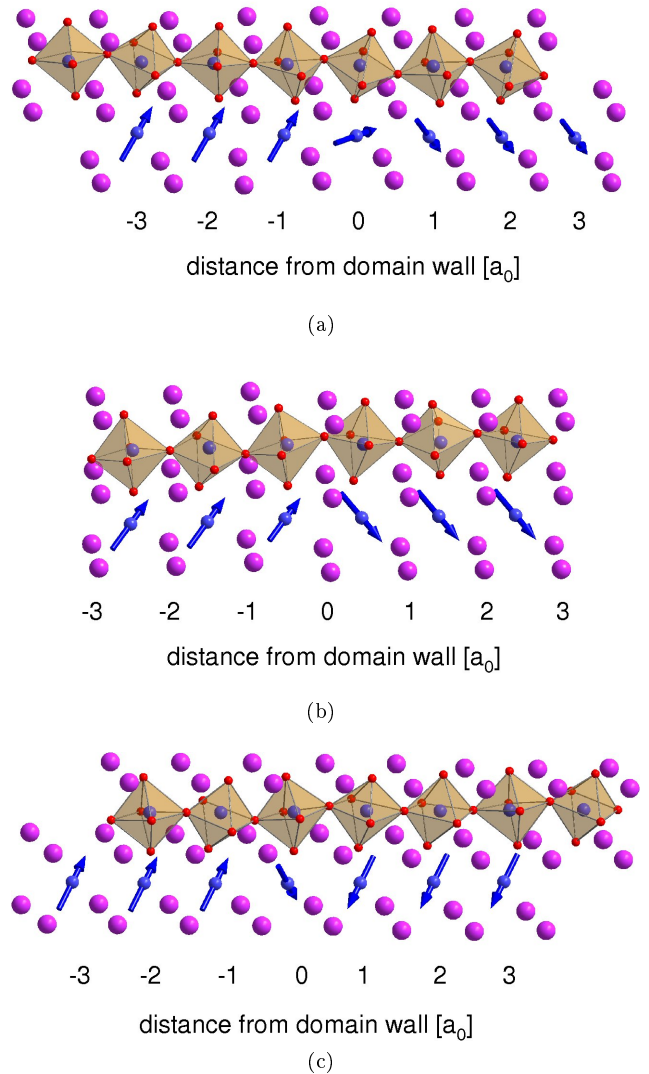


FIG. 6: Evolution of the local polarization across (a) the 71°, (b) the 109° and (c) the 180° domain wall. The blue arrows represent the magnitude and orientation of the local polarization.

### C. Electronic properties of the domain walls

In light of the intriguing reported electrical conductivity mentioned above, we next analyze the electronic properties of the domain walls. We look particularly at the layer-by-layer densities of states, to see if the structural deformations in the wall region lead to a closing of the electronic band gap. Indeed, earlier DFT calculations for bulk  $\text{BiFeO}_3$  [4] indicated a strong dependence of the electronic band gap on the structure. In particular the ideal cubic structure, in which the 180° Fe-O-Fe bond angles maximize the Fe 3d - O 2p hybridization and hence the bandwidth, has a significantly reduced band gap compared with the  $R3c$

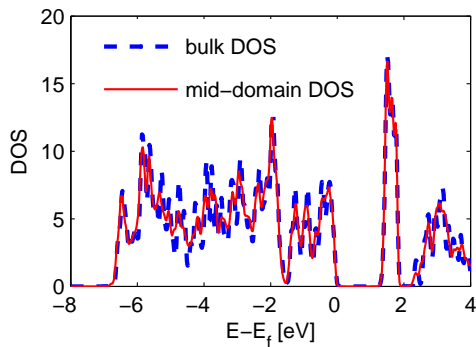


FIG. 7: Comparison of calculated bulk DOS for  $\text{BiFeO}_3$  (dashed line) with the local density of states of a mid-domain layer in the supercell with a  $109^\circ$  domain wall. The sum of both spin channels is shown.

structure and is even metallic within the LSDA.

First, in Figure 7 we compare the local density of states (LDOS) for a layer in the center of a domain with our calculated density of states for bulk  $\text{BiFeO}_3$ . The mid-domain LDOS shown is for the supercell containing the  $109^\circ$  wall; those of the  $71^\circ$  and  $180^\circ$  supercells are indistinguishable. As found in prior work [4], the bulk valence band consists of O  $2p$  - majority spin Fe  $3d$  hybridized states, while the bottom part of the conduction band is formed of minority spin Fe  $3d$  states and Bi  $6p$  states. The LSDA+ $U$  band gap is 1.4 eV for our chosen values of  $U$  and  $J$ . The electronic structure in the mid-domain region fully recovers the bulk behavior.

In the domain wall, deformation of the Fe-O-Fe angles causes changes in the hybridization which affect the Fe  $e_g$  states, resulting in shifts of the band edges. These are strongest at the  $180^\circ$  boundary where the deformations are largest and the Fe-O-Fe angles are strongly increased. Fig. 8 compares the mid-domain and domain wall LDOSs for the three wall orientations. The increasing downward shift in the conduction band edge from  $71^\circ$  to  $109^\circ$  to  $180^\circ$  walls, correlating with the increasing change in Fe-O-Fe band angle is clearly visible. At the  $180^\circ$  wall there is an additional shift of the top of the valence band (consisting of O  $2p$  - Fe  $3d$  hybridized states) upwards in energy. These band edge shifts in turn cause a reduction in the local band gap, which is plotted in Fig. 9. Again the change is smallest for the  $71^\circ$  wall and largest for the  $180^\circ$  wall.

In Fig. 9 we show the local band gap extracted from the layer-by-layer densities of states across the three wall types. In all cases we see a reduction in the band gap in the wall region, with the  $180^\circ$  wall again showing the largest effect. In no case, however, does the gap approach zero in the wall region.

Finally, to provide a quantitative measure of the extent of localization of the states near the conduction band edge, we calculate the projection of the lowest energy

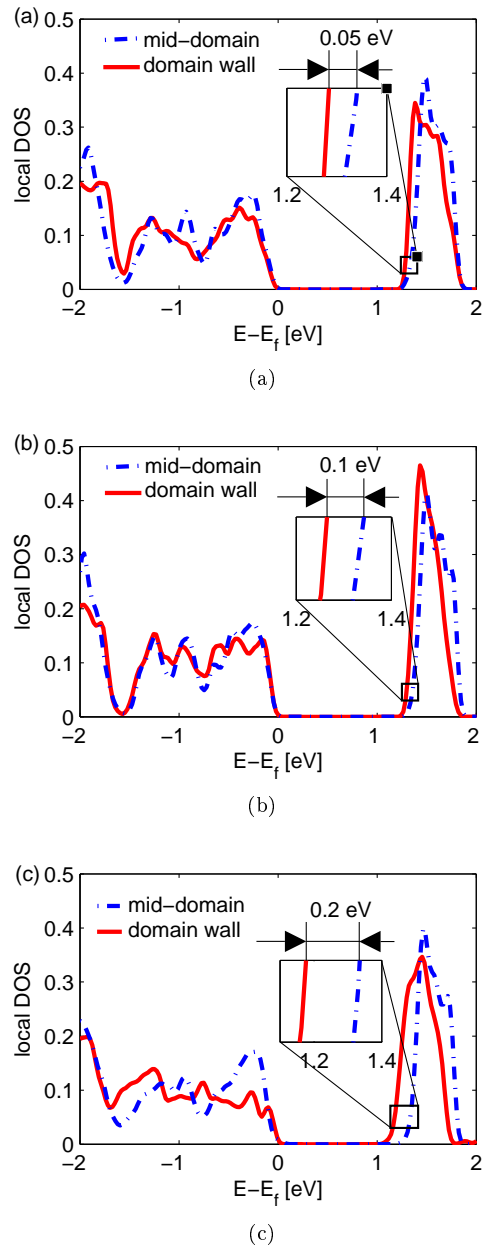


FIG. 8: Comparison of the calculated Fe LDOS in the mid-domain and domain wall regions for (a)  $71^\circ$ , (b)  $109^\circ$  and (c)  $180^\circ$  walls. Note the downward shifts in the conduction band edges, particularly in the  $109^\circ$  and  $180^\circ$  cases. The  $180^\circ$  case also shows a small upward valence band edge shift.

conduction band onto each layer of the supercell; our results are shown in Figure 10. It is clear that the conduction band edge is dominated by states in the domain wall, more so in the  $109^\circ$  wall (on the  $\{100\}$  plane) than in the  $71^\circ$  and  $180^\circ$  walls (which are both in  $\{110\}$  planes). Again, this implies that electron carriers in the system, which will occupy the lowest conduction band states, will accumulate at the domain boundary regions.



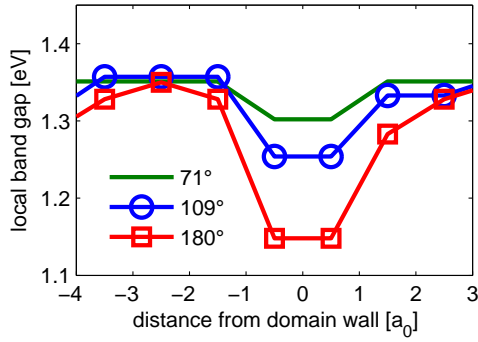


FIG. 9: Local band gap extracted from the layer-by-layer densities of states.

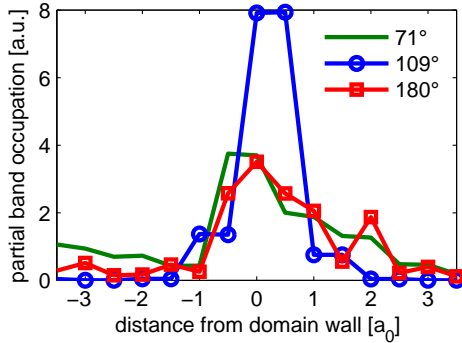


FIG. 10: Layer-by-layer projection of the lowest conduction band (partial band occupation) for 71°, 109° and 180° domain walls. The integrated partial band occupation is equal to one.

#### D. Magnetic properties

In bulk  $\text{BiFeO}_3$ , the magnetic ordering is G-type antiferromagnetic with a long wavelength ( $\sim 620$  Å) spiral of the AFM axis [13]. The spiral is known to be suppressed by doping [23] and importantly for this work is believed to be suppressed in thin films [24]. Our earlier first-principles calculations showed that the AFM vector lies in one of six easy axes within the magnetic easy plane which is perpendicular to the polar axis. We found a spin-orbit driven canting of the magnetic moments of  $\sim 1^\circ$  [14] which, in the absence of a spiral, results in a net weak ferromagnetism of  $0.05 \mu_B$  per Fe ion. The canting is symmetry allowed because of the octahedral rotations; a hypothetical  $R3m$  polar structure without octahedral rotations could not show weak ferromagnetism. Recent magneto-optical measurements showed the antiferromagnetism can be controlled using an electric field because its orientation is determined by the direction of the ferroelectric polarization [1].

In this final section we include spin-orbit coupling in our calculations in order to explicitly calculate the orientation of the magnetic moments relative to the

polarization vector, and to allow any spin-orbit driven canting to manifest. Consistent with Ref. [24] and for computational feasibility, we use the ideal G-type structure with initial spin polarization axis set to the pseudocubic  $[1\bar{1}0]$  direction, which was chosen because it is perpendicular to the electric polarization vectors on both sides of the domain wall ( $[111]/[\bar{1}\bar{1}\bar{1}]$  in the  $109^\circ$  case) as our starting point; we do not allow the long wavelength spiral. Since the non-collinear calculations with spin-orbit coupling are so computationally intensive, we are only able to study one wall orientation. We choose to study the  $109^\circ$  wall since it is accompanied by a reorientation of the antiferromagnetic easy plane across the boundary; our findings might also be applicable to the  $71^\circ$  domain wall in which the easy plane also reorients across the boundary. (At the  $180^\circ$  domain wall the polarization reverses direction and so we expect the easy plane of magnetization, which is perpendicular to the polarization, to remain unchanged across the domain wall. In addition, since our structural studies described above found that the phase of the octahedral rotations – which determines the orientation of the canting – is unchanged across the domain wall, we do not expect a reversal of the weak ferromagnetic vector.) We expect that changes in the local symmetry at the wall might significantly affect the canting angles; in addition if the perturbations in the Fe-O-Fe bond angles are large enough we could even see a change from antiferromagnetic to ferromagnetic superexchange [25, 26, 27].

In Fig. 11 we show the net local magnetization resulting from the canting of the Fe magnetic moments in each layer across the  $109^\circ$  domain wall. In the mid-domain regions the orientation of the local moment is  $[11\bar{2}]$  on one side and  $[\bar{1}\bar{1}2]$  on the other side of the wall. The magnitude of the local moment is consistent with that calculated for bulk  $\text{BiFeO}_3$ . The reorientation of the AFM plane consistent with the reorientation of the polarization is evident. Importantly, we see that the local canting *increases* by  $\sim 33\%$  in the wall layer, consistent with the larger deviation of the Fe-O-Fe angles from  $180^\circ$ . This behavior could explain the intriguing recent observation that the magnitude of the exchange bias in  $\text{BiFeO}_3/\text{Co}$  multilayers is affected by the ferroelectric domain structure in  $\text{BiFeO}_3$  [28].

## VI. SUMMARY

In summary, we have used the LSDA+ $U$  method of density functional theory to calculate the structural, electronic and magnetic properties of the ferroelectric domain walls in multiferroic  $\text{BiFeO}_3$ . We have identified the wall orientations that are most likely to occur based on their relative energy costs; in particular we have shown that walls in which the rotations of the oxygen octahedra



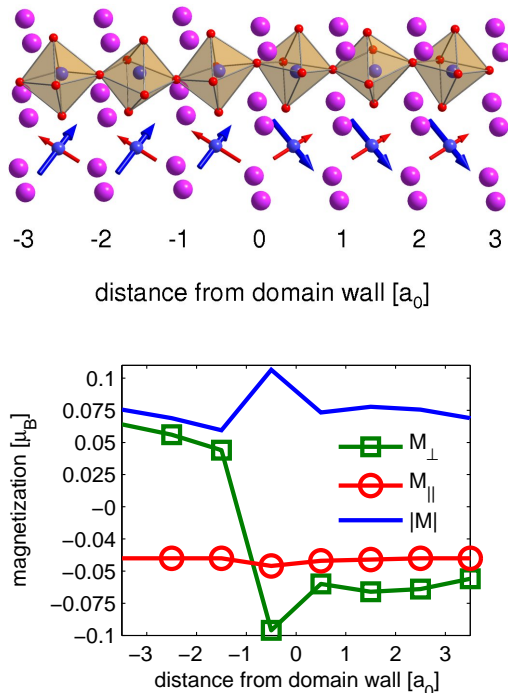


FIG. 11: Layer-by-layer local magnetic moment across the 109° domain boundary. (a) Shows the local magnetization vectors (small red arrows) resulting from the canting of the Fe magnetic moments in each layer, which is perpendicular to the local electric polarization (big blue arrow), (b) shows the local component of the magnetization projected parallel and perpendicular to the wall plane, and the local magnitude.

do not change their phase when the polarization reorients are significantly more favorable than those with rotation discontinuities. Our analysis of the local polarization and electronic properties revealed potential steps and reduction in local band gaps at the 109° and 180° walls; these correlated with recent measurements of electrical conductivity at these boundaries. Finally, we showed that changes in structure at the domain walls cause changes in canting of the Fe magnetic moments which can enhance the local magnetization at the domain walls. The latter suggests possible new routes to electric field-control of magnetism in BiFeO<sub>3</sub>.

## VII. ACKNOWLEDGMENTS

Spaldin was supported by the National Science Foundation under Award No. DMR-0605852. Calculations were performed at the San Diego Supercomputer Center, and at the National Center for Supercomputer Applications. We furthermore acknowledge the DFG for funding through FOR 520 and Ge 1202/5-1 and the BMBF for funding via the Pakt fuer Forschung und Innovation.

\* Electronic address: axel.rother@triebenberg.de

† Electronic address: s.gemming@fzd.de

‡ Electronic address: nicola@mrl.ucsb.edu

- [1] T. Zhao, A. Scholl, F. Zavaliche, K. Lee, M. Barry, A. Doran, M. P. Cruz, Y. H. Chu, C. Ederer, N. A. Spaldin, et al., *Nature Mater.* **5**, 823 (2006).
- [2] Y.-H. Chu, L. W. Martin, M. B. Holcomb, M. Gajek, S.-J. Han, Q. He, N. Balke, C.-H. Yang, D. Lee, W. Hu, et al., *Nature Mater.* **7**, 478 (2008).
- [3] J. Wang, J. B. Neaton, H. Zheng, V. Nagarajan, S. B. Ogale, B. Liu, D. Viehland, V. Vaithyanathan, D. G. Schlom, U. V. Waghmare, et al., *Science* **299**, 1719 (2003).
- [4] J. B. Neaton, C. Ederer, U. V. Waghmare, N. A. Spaldin, and K. M. Rabe, *Phys. Rev. B* **71**, 014113 (2005).
- [5] S. Stemmer, S. K. Streiffer, F. Ernst, and M. Rühle, *Philos. Mag. A* **71**, 713 (1995).
- [6] N. Floquet and C. Valot, *Ferroelectrics* **234(1-4)**, 107 (1999).
- [7] J. Padilla, W. Zhong, and D. Vanderbilt, *Phys. Rev. B* **53**, R5969 (1996).
- [8] B. Meyer and D. Vanderbilt, *Phys. Rev. B* **65**, 104111 (2002).
- [9] J. Seidel, L. W. Martin, Q. He, Q. Zhan, Y.-H. Chu, A. Rother, M. E. Hawkrige, P. Maksymovych, P. Yu, M. Gajek, et al., *Nat Mater* **8**, 229 (2009), ISSN 1476-1122, URL <http://dx.doi.org/10.1038/nmat2373>.
- [10] C. J. Fennie, *cond-mat/0807.0472* (2008).
- [11] F. Kubel and H. Schmid, *Acta Crystallogr. B* **46**, 698 (1990).
- [12] P. Fischer, M. Polemska, I. Sosnowska, and M. Szymański, *J. Phys. C* **13**, 1931 (1980).
- [13] I. Sosnowska, T. Peterlin-Neumaier, and E. Streichele, *J. Phys. C* **15**, 4835 (1982).
- [14] C. Ederer and N. A. Spaldin, *Phys. Rev. B* **71**, 060401(R) (2005).
- [15] C. J. Fennie, *Phys. Rev. Lett.* **100**, 167203 (2008).
- [16] S. K. Streiffer, C. B. Parker, A. E. Romanov, M. J. Lefevre, L. Zhao, J. S. Speck, W. Pompe, C. M. Foster, and G. R. Bai, *Journal of Applied Physics* **83** Nr. 5, 2742 (1998).
- [17] G. Kresse and J. Furthmüller, *Comput. Mater. Sci.* **6**, 15 (1996).
- [18] P. E. Blöchl, *Phys. Rev. B* **50**, 17953 (1994).
- [19] G. Kresse and D. Joubert, *Phys. Rev. B* **59**, 1758 (1999).
- [20] A. I. Liechtenstein, V. I. Anisimov, and J. Zaanen, *Phys. Rev. B* **52**, R5467 (1995).
- [21] V. I. Anisimov, F. Aryasetiawan, and A. I. Liechtenstein, *J. Phys.: Condens. Matter* **9**, 767 (1997).
- [22] C. Ederer and N. A. Spaldin, *Phys. Rev. B* **71**, 224103 (2005).
- [23] I. Sosnowska, W. Schäfer, W. Kockelmann, K. H. Andersen, and I. O. Troyanchuk, *Appl. Phys. A* **74**, S1040 (2002).
- [24] F. Bai, J. Wang, M. Wuttig, J. Li, N. Wang, A. P. P. dn A. K. Zvezdin, L. E. Cross, and D. Viehland, *Appl. Phys. Lett.* **86**, 32511 (2005).
- [25] J. Kanamori, *J. Phys. Chem. Solids* **10**, 87 (1959).
- [26] P. W. Anderson, in *Magnetism*, edited by G. T. Rado and H. Suhl (Academic Press, 1963), vol. 1, chap. 2, pp. 25–83.

- [27] J. B. Goodenough, *Magnetism and the Chemical Bond* (Interscience Publishers, New York, 1963).
- [28] L. W. Martin, Y.-H. Chu, M. B. Holcomb, M. Huijben, P. Yu, S.-J. Han, D. Lee, S. X. Wang, and R. Ramesh, *Nanoletters* **8**, 2050 (2008).